Materials Science & Engineering A 949 (2026) 149422

Contents lists available at ScienceDirect

Materials Science & Engineering A

journal homepage: www.elsevier.com/locate/msea

Role of nanotwins, stacking faults, and short-range order in strengthening CoCrNi medium-entropy alloys: An atomistic modeling study

Charles Matlock, Ning Zhang *

Department of Mechanical Engineering, Baylor University, Waco, TX, 76706, USA

ARTICLE INFO

Keywords:
Medium entropy alloy
Twinning
Stacking fault
Short-range order
Molecular dynamics

ABSTRACT

CrCoNi medium-entropy alloys (MEAs) are renowned for their exceptional mechanical properties, yet the strengthening mechanisms associated with planar defects and chemical short-range order (SRO) remain incompletely understood. In this work, we employ large-scale molecular dynamics simulations to systematically investigate the effects of nanotwins, stacking faults (SFs), and SRO on the deformation behavior and mechanical response of polycrystalline CrCoNi MEAs. Stress–strain analyses reveal that both nanotwins and SFs markedly enhance strength and energy absorption, although through different mechanisms: nanotwins confine and disrupt dislocation glide while promoting FCC–HCP phase transformations, whereas SFs suppress dislocation nucleation and propagation, with narrower inter-fault spacing providing stronger barriers to plastic flow. Among planar defects, the two-atomic-layer twin and six-atomic-layer SF configurations exhibit the most pronounced strengthening, enhancing strength by 16 % and 13 %, respectively. Beyond these effects, SRO exerted a dominant strengthening effect, increasing strength by 45 %, stiffness by nearly 30 %, and energy absorption by 50 %. With the additional contribution of gradient twins, strength enhancement reaches 57 %. Mechanistically, SRO stabilizes defect boundaries via Ni segregation, promotes nanograin coalescence and lattice adjustment that reduce grain boundary density, and significantly suppresses dislocation activity. These findings highlight the synergistic contributions of nanotwins, SFs, and SRO to the extraordinary strength-ductility synergy of CrCoNi MEAs, providing mechanistic insight for defect- and chemistry-engineered design of high-performance alloys.

1. Introduction

High entropy alloys (HEAs) are typically defined as alloys with a configurational entropy greater than 1.5R (where $R = 8.314\ J/K\ mol^{-1}$), while medium entropy alloys (MEAs) exhibit configuration entropies between 1.2R and 1.5R [1,2]. Among these alloys, the ternary CrCoNi MEA demonstrates an outstanding combination of properties, including high strength, ductility, and fracture toughness, particularly at cryogenic temperatures, surpassing most other MEAs and HEAs [1,3–6].

Polycrystalline CrCoNi MEAs are conventionally fabricated by vacuum arc melting followed by drop casting, homogenization annealing, cold rolling, and recrystallization to achieve a uniform microstructure [7]. However, this process often introduces casting-related defects such as porosity, elemental segregation, inclusions, coarse grains, dislocations, nanotwins, and stacking faults (SFs), many of which can substantially deteriorate the mechanical performance of the alloy. For example, significant deformation twinning (DT) was observed in as-cast CrCoNi alloys, and it is prevalent with decreasing temperature [6,8,9]. Significant partial dislocation slips and deformation-induced phase transformation were revealed by transmission electron microscopy (TEM) [5,10–12]. With the advancement of modern processing techniques, including laser-aided additive manufacturing [13], such drawbacks can be mitigated by reducing both the size and number of defects.

Interestingly, it was found that certain processing-induced defects, such as dislocation cell walls and nano-inclusions, can significantly enhance the yield strength. Subsequently, new fabrication and post-processing thermomechanical methods, such as rolling and annealing, have been developed to tailor the microstructure [13–15]. These approaches include recrystallization, grain refinement, and the controlled formation of beneficial planar defects, such as SFs, twins, and secondary phases. Such defects can be utilized to further enhance the strength and ductility of alloys. For instance, hot rolling has been demonstrated to be effective in reducing or even eliminating microstructural defects, triggering dynamic recrystallization and refining grains, thereby enhancing alloy strength [16].

Furthermore, the strategy of introducing minor alloying additions to

* Corresponding author.
E-mail address: Ning_Zhang@baylor.edu (N. Zhang).

https://doi.org/10.1016/j.msea.2025.149422
Received 25 September 2025; Received in revised form 2 November 2025; Accepted 5 November 2025
Available online 6 November 2025

promote the formation of such defects has been widely investigated, primarily through experimental studies. This strategy has been demonstrated to be effective in promoting the formation of desirable defects and improving the mechanical properties of CrCoNi MEAs. For instance, the addition of 6.26 at% Mo resulted in significant grain refinement, which in turn led to a remarkable increase in hardness, yield strength, and ultimate tensile strength, albeit accompanied by a pronounced reduction in ductility [7]. Similarly, the addition of Si has been reported to reduce the stacking-fault energy (SFE), thereby promoting deformation twinning and enhancing steady strain hardening [13]. Consequently, strengthening dislocation-twin and dislocation-dislocation reactions like Lomer-Cottrell (LC) locks have been reported because of the low SFE in CrCoNi MEA [5,9,17]. When the CoCrFeNi HEA was doped with a small amount of Cu (2 at. %), an FCC-to-HCP phase transformation was detected, which thereby enhanced the strength of the alloy through synergistic effects of dislocation, heterogeneous deformation, and phase transformation-induced plasticity (TRIP). It has been reported that hcp lamellae can form under various deformation conditions, with their widths and interspacing varying accordingly [9,18].

For a long time, HEAs and MEAs have been viewed as possessing a highly ordered lattice structure yet exhibiting significant chemical disorder. However, experimental [19–22] and computational [23,24] studies have now provided substantial evidence for the pervasive existence of nanoscale short-range order (SRO), the formation of which is believed to be driven by the competition between enthalpy and entropy [25]. The emergence of SRO was shown to enhance the strength of alloys, which is probably by influencing the SFE, adjusting phase transformation energy barriers, and increasing resistance to dislocation motion. Computationally, great efforts have been devoted to simulating the formation of SRO and its impact on the properties of MEAs [26]. In our previous work, a hybrid Monte Carlo (MC) and molecular dynamics (MD) simulation approach was employed to simulate the formation of SRO in single-crystalline CrCoNi MEA [27]. The results revealed that SRO markedly enhances the strength, stiffness, and energy absorption capability of the alloy. The underlying strengthening mechanisms were identified as modifications to the formation pathways of twins and SFs, as well as an increased propensity for deformation twinning, which are consistent with experimental observations [28].

While the strengthening effects of individual defects such as nanotwins, SFs, and SRO have been studied separately, the combined influence of these mechanisms and their dependence on defect width, density, and spatial distribution remain unclear. Because these hierarchical mechanisms interact, isolating their respective contributions to mechanical enhancement is difficult to achieve experimentally. In this study, large-scale MD simulations are employed to elucidate the effects of nanotwins, SFs, and SRO on the deformation behavior of polycrystalline CrCoNi MEAs, quantitatively assessing their individual and synergistic contributions to strengthening.

2. Methodology

2.1. Model generation

To study the effect of lattice defects on the mechanical properties of CrCoNi alloys, such as yield and ultimate strength, atomistic simulations were conducted using LAMMPS with GPU acceleration [29,30]. Polycrystalline models with nano-sized grains were employed to balance computational feasibility and physical relevance, consistent with experimentally observed nanostructured CrCoNi MEAs [6,31–33]. Six models were constructed with pre-introduced defects of nano-twinning and stacking faults with featuring varied parameters, including width and interspacing, as representatively illustrated in Fig. 1. The 3D polycrystalline models were generated using AtomSK [34], and subsequently visualized and analyzed with Ovito Pro [35,36]. The models were

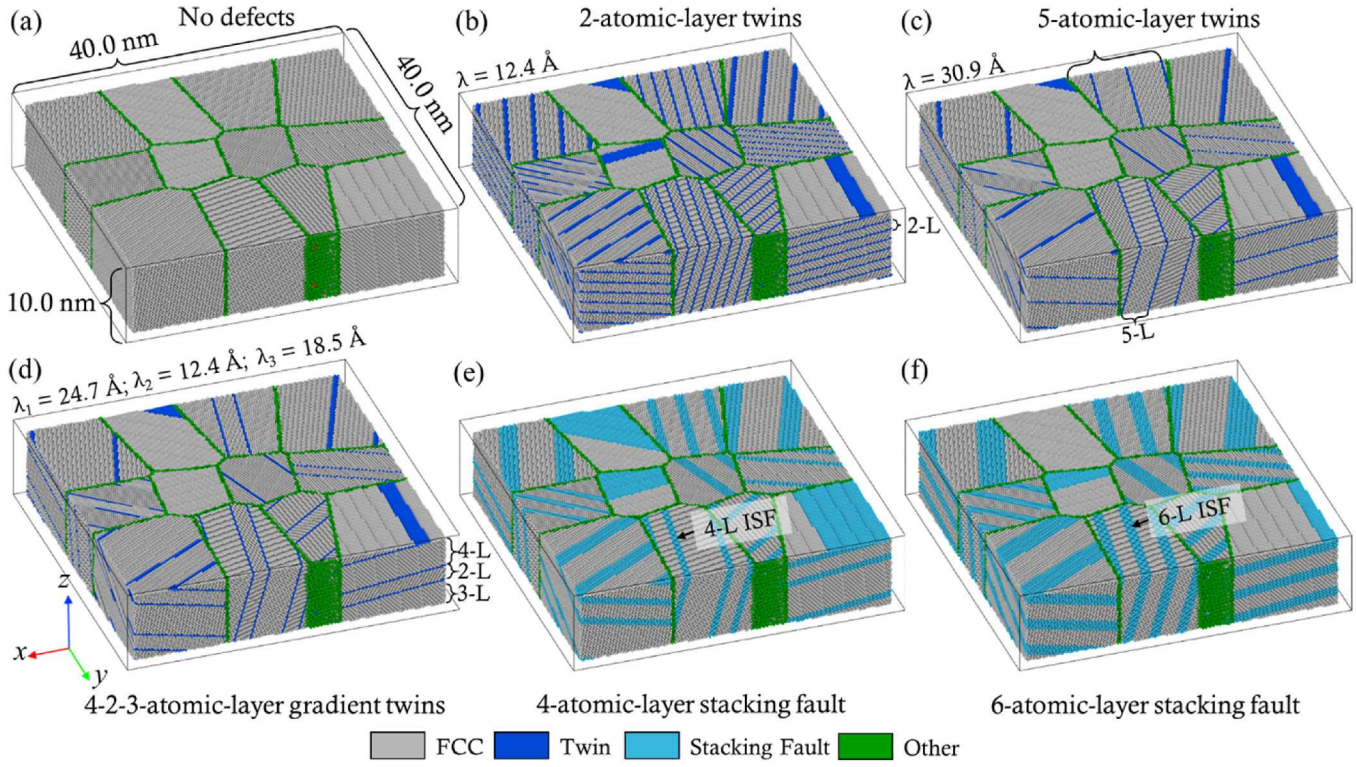

Fig. 1. 3D polycrystalline models of equiatomic CrCoNi MEA. (a) Defects-free model. (b–c) Models with uniformly distributed nanotwins of different widths, corresponding to two and five atomic layers (λ = 12.4 Å and 30.9 Å, respectively). (d) Model with gradient twin widths in the pattern of 4-2-3 atomic layers (λ = 24.7 Å, 12.4 Å, and 18.5 Å). Models with SFs of widths corresponding to (e) four atomic layers (λ = 24.7 Å) and (f) six atomic layers (λ = 37.2 Å). To clearly illustrate GBs and introduced defects, different elements were not distinguished by color. Gray atoms represent the FCC lattice, dark blue atoms denote nanotwins, light blue atoms indicate SFs, and green atoms denote GBs. (For interpretation of the references to color in this figure legend, the reader is referred to the Web version of this article.)

constructed with dimensions of 40.0 nm × 40.0 nm × 10.0 nm and approximately 1,400,000 atoms to represent a columnar grain structure (Fig. 1a). Each model consisted of twelve nanograins with an average diameter of ~10.0 nm. Boundary conditions were set to periodic to reduce the effects related to the geometry of the model and represent a small plate section inside of a larger section of polycrystalline material, a method employed in many MD studies of polycrystalline materials [26, 37–39]. Each generated grain was assigned a unique crystallographic orientation, ensuring that neighboring grains across periodic boundaries remained distinct and formed well-defined grain boundaries rather than combining into a single grain. To minimize potential bias arising from a specific microstructural configuration on the predicted mechanical properties and associated mechanisms, ten independent models were generated with identical dimensions, grain numbers, and average grain size but with random grain shapes, distributions, and orientations. The polycrystalline model shown in Fig. 1 is provided as a representative example. Each model was constructed with a random equiatomic composition of Cr, Co, and Ni (1/3 each) and employed a lattice constant of 3.567 Å [6]. The Embedded Atom Method (EAM) potential developed by Li et al. [23] was employed, as it has been shown to reliably capture SRO deformation behavior and mechanical properties, as demonstrated in our previous study [27], and in other reported studies [40–42].

To investigate the effect of nanotwins, three twinning configurations were constructed: two models with uniformly spaced twins and a third with a gradient twin structure. The nanotwins investigated were assigned a range of widths (λ) and oriented along the <112> crystallographic direction, consistent with the slip of Shockley partial dislocations. In CrCoNi MEAs, deformation twinning typically initiates on {111} planes via the nucleation of Shockley partial dislocations [31,43]. The widths of the nanotwins were set to be $\lambda_{2L} = 1.24$ nm, $\lambda_{3L} = 1.85$ nm, $\lambda_{4L} = 2.47$ nm, and $\lambda_{5L} = 3.1$ nm for the 2-atomic-layer twin (2-LT), 4-2-3-atomic-layer gradient twin (4-2-3-GT), and the 5-atomic-layer (5-LT) twin, respectively. The effect of SFs was further studied using models with 4-atomic-layer (4-LSF) and 6-atomic-layer SFs (6-LSF), corresponding to two and three intrinsic stacking faults (ISF), here referred to as multilayer stacking faults (MSF).

All inserted twins and stacking faults were generated using AtomSK's built-in tools for defect construction, implemented through custom batch scripts to streamline model creation [34]. The procedure follows the methodology described in the AtomSK documentation. Each twinned configuration was constructed starting from a single-crystal lattice containing the specified number of atomic layers for the intended twin variant. The single-crystal model was mirrored and merged to form a twin boundary, and this process was repeated to achieve the desired twin density. The resulting twinned model was then used as the input for AtomSK's Voronoi polycrystal generator to produce polycrystalline structures with the specified twin distribution.

Similarly, stacking fault (SF) configurations were generated from single-crystal lattices by bisecting the structure and introducing an atomic shift equivalent to one Burgers vector along the <112> direction on the {111} plane, corresponding to the partial dislocation vector of the alloy. The procedure was repeated to obtain the desired number of SF layers. The SF-embedded single crystals were then inserted into the Voronoi algorithm to produce polycrystalline models containing predefined SF structures. This systematic approach for introducing planar defects using AtomSK has been widely adopted in molecular dynamics studies investigating defect-mediated deformation mechanisms in metallic materials [44–46].

2.2. Short-range order (SRO) generation

To study the effects of SRO on the mechanical properties of models containing planar lattice defects, hybrid molecular dynamics-Monte Carlo (MD-MC) simulations were performed using the variance-constrained semi-grand canonical (VC-SGC) ensemble [47]. This approach involves iterative isothermal-isobaric (NPT) quenching, chemical potential differences setup, and evaluation of SRO degree by Warren-Cowley parameters [48]. Further details of the SRO generation procedure are available in our previous work [27]. For models with defects included, the final polycrystalline models created using AtomSK were then placed through the SRO generation algorithm.

2.3. Simulation details

The simulations were performed under full periodic boundary conditions using the NPT ensemble with zero normal pressure. The initial models were first subjected to a conjugate-gradient minimization, followed by relaxation at 298 K for 100 ps. Tensile loading was applied at a constant uniaxial strain rate of 5×10^8 s^{-1} up to a final strain of 25 %, ensuring minimization of numerical artifacts [49,50]. The velocity–Verlet algorithm [51] was utilized with a timestep of 1 fs for the integration of the equations of motion. The stress-strain curve of each model was plotted, and the Young's modulus was determined as the slope of the elastic portion of the stress-strain curve. Yield strength was identified as the peak stress, as no obvious strain-hardening beyond yielding was observed. The relative toughness was evaluated by calculating the energy absorption capability, defined as the area under the entire stress-strain curve. Additionally, for each defected configuration, mean values of the mechanical properties were calculated for comparison. The polycrystalline model exhibiting the best mechanical properties was selected for subsequent SRO simulations and for visualization of the deformed structure.

2.4. Deformation mechanism analysis

Crystal structures were characterized using common neighbor analysis (CNA) and polyhedral template matching, while dislocations were identified with the dislocation extraction algorithm (DXA) [10]. Planar SFs were detected and visualized using OVITO Pro and quantified through custom Python scripts [11]. For each deformation mechanism, the number of associated atoms was tracked as a function of applied strain. In models containing pre-existing defects, atoms belonging to the initial defects were excluded from the analysis to ensure only newly formed deformation mechanisms were considered. The contribution of each mechanism to strain accommodation was quantified using custom Python scripts by calculating the fraction of total strain accommodated. Specifically, the strain tensor along the loading direction for atoms within each mechanism was determined and expressed as a percentage of the total strain tensor of all atoms, following the methodology of Gupta et al. [26]. The curves were plotted using custom MATLAB codes.

3. Results & discussion

3.1. Effects of nanotwins and stacking faults on mechanical properties

Fig. 2 presents the stress–strain curves for each defect type across the ten polycrystalline models. Considerable variation in mechanical response is observed among models with the same defect type but different polycrystalline structures, with model-2 (orange curves in Fig. 2a–f) exhibiting the highest strength across all defective cases. To facilitate comparison, Fig. 3a shows the mean stress–strain responses, while Fig. 3b highlights the responses of model-2, which was selected as a representative case for subsequent deformation mechanisms analysis. In general, the stress–strain curves for all defect types exhibit a sharp rise to yield, followed by a stress drop and a plateau region during continued plastic flow. The immediate post-yield behavior is particularly informative, as it reflects the rate of dislocation nucleation.

As shown in Fig. 3b, the model with 2-LTs exhibited the most pronounced stress reduction after yielding, indicative of a more brittle-like response and rapid, relatively unconstrained dislocation nucleation. In contrast, the model with 4-LSFs displayed the smallest post-yield stress drop, reflecting a comparatively ductile response. Among the twinned

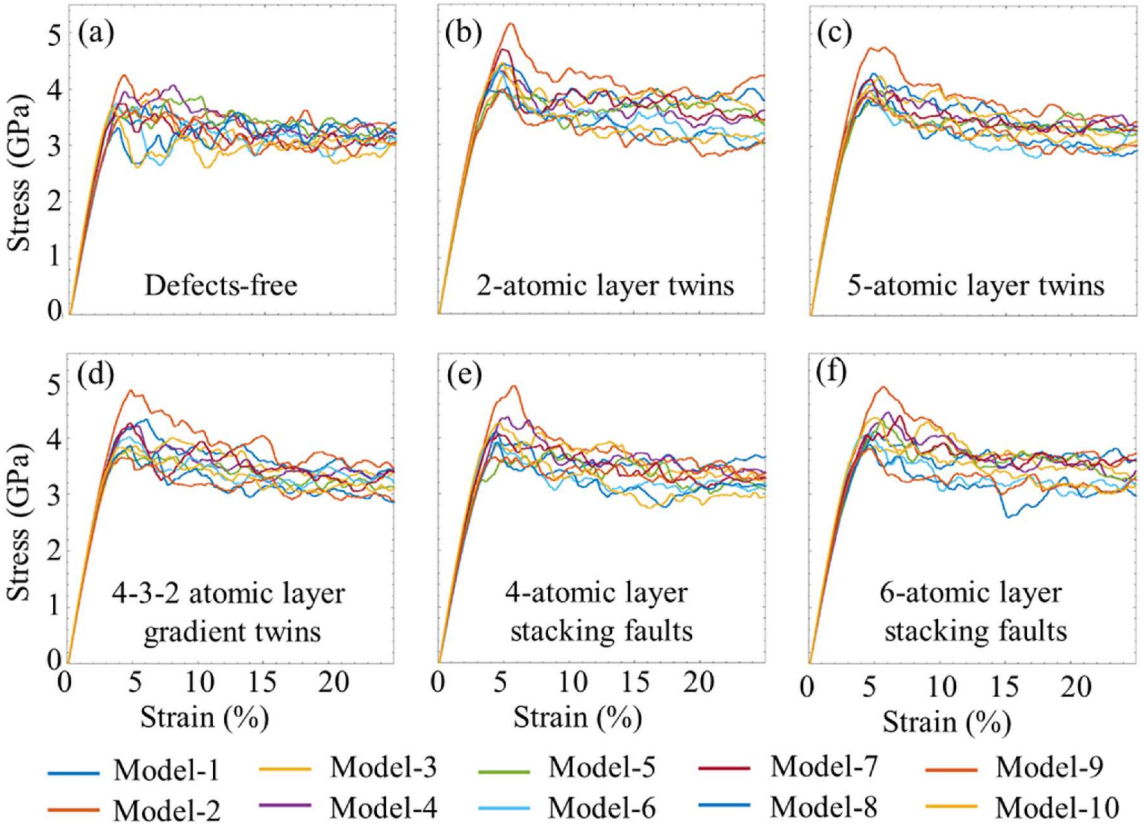

Fig. 2. Stress-strain responses of polycrystalline CrCoNi MEAs with different defect types. For each configuration, ten independent polycrystalline models with identical dimensions, number of grains, and average grain size but random nanograin shapes and orientations were tested to minimize bias from any specific microstructural case. Stress-strain curves of CrCoNi with (a) no defects, (b) 2-atomic-layer twins, (c) 5-atomic-layer twins, (d) 4-2-3-atomic-layer gradient twins, (e) 4-atomic-layer SFs, and (f) 6-atomic-layer SFs. The stress-strain curves of the ten polycrystalline models in each case are distinguished by different colors. (For interpretation of the references to color in this figure legend, the reader is referred to the Web version of this article.)

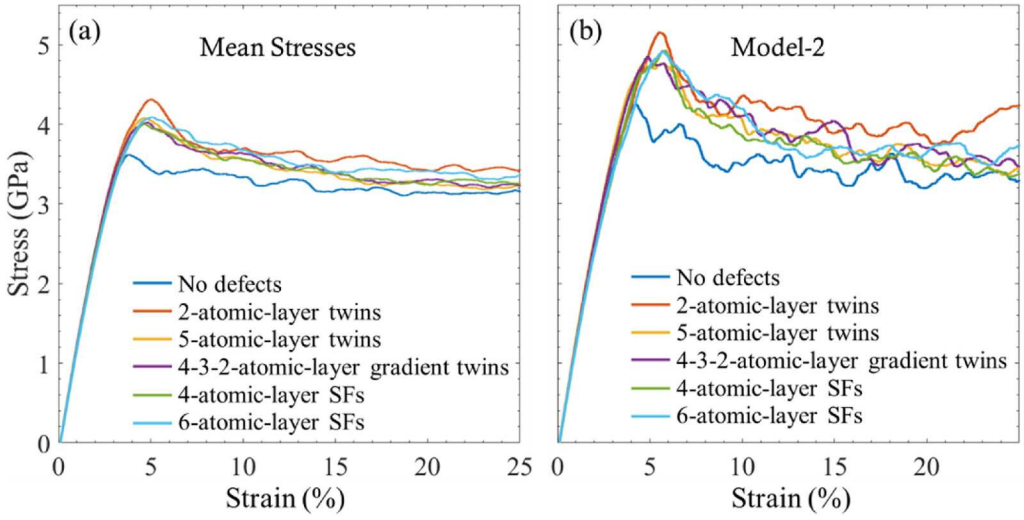

Fig. 3. (a) Mean stress-strain curves of the six cases shown in Fig. 2. (b) Representative stress-strain curves of polycrystalline model-2 with different defect types.

cases, the 4-2-3-GT configuration showed the least stress reduction, suggesting improved resistance to abrupt dislocation activity.

The mechanical responses of the models are summarized in Fig. 4. A slight reduction in elastic modulus is observed with the introduction of defects, decreasing from 122.3 GPa in the defect-free model to 117.1 GPa in the 6-LSF case. In contrast, the addition of nanotwins and stacking faults (SFs) produces significant enhancements in yield strain, strength, and energy absorption. Among these, the 2-LT configuration exhibits the most pronounced improvements in strength (16 %) and energy absorption (10 %). It is noteworthy that decreasing the twin width increases the total number of twins introduced, suggesting that the number of twins has a greater influence on raising the critical stress required for dislocation motion than twin width alone. Similarly, the 6-LSF case demonstrates higher strength (13 % enhancement) compared

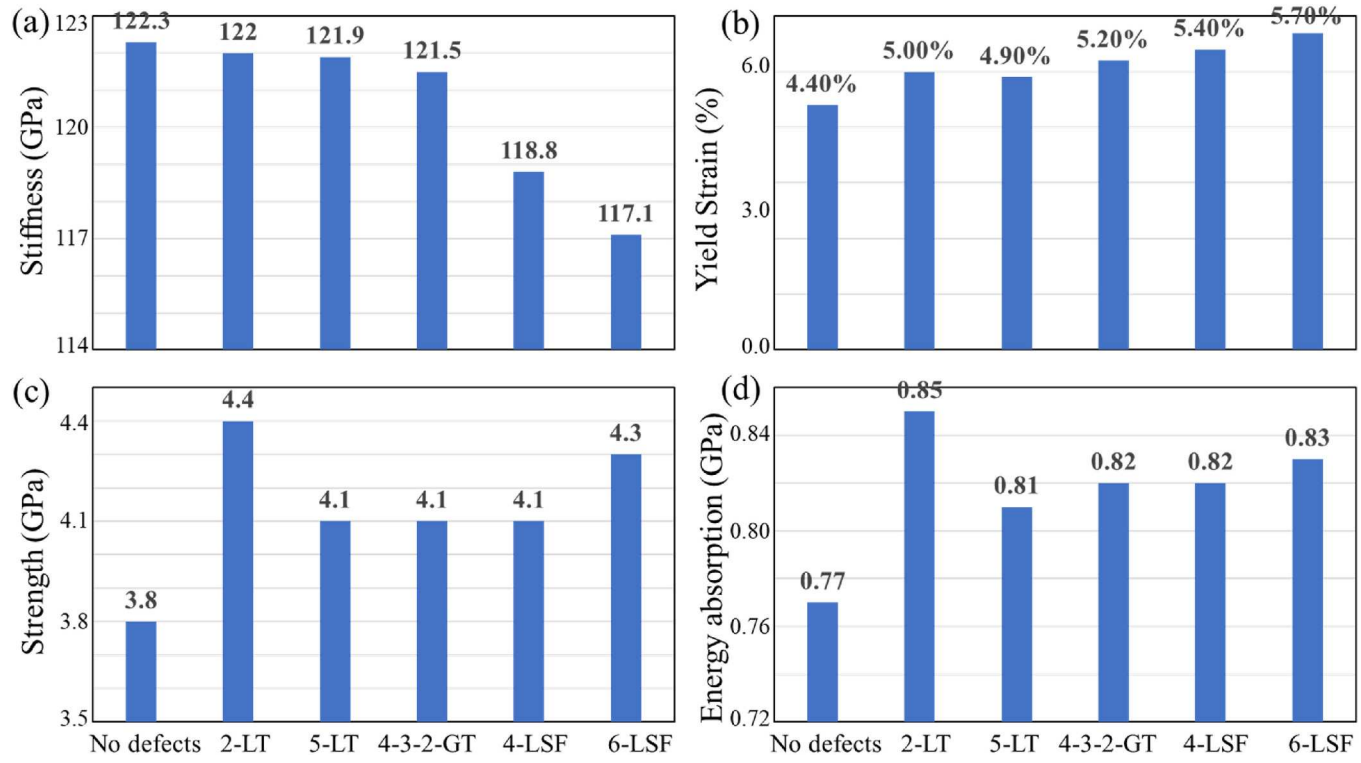

Fig. 4. Bar chart comparison of the mean mechanical properties of polycrystalline CrCoNi with different defect types: (a) stiffness, (b) yield strain, (c) strength, and (d) energy adsorption. The data were derived from the mean stress-strain curves in Fig. 3a.

to the 4-LSF case, highlighting the role of wider SFs in elevating the critical stress for dislocation nucleation.

Defects also delay yielding relative to the defect-free model. Although the differences in yield strain among defect types are modest, the 6-LSF case achieves the largest yield strain, whereas the 2-LT case exhibits the smallest. While the 2-LT configuration delivers the greatest strengthening, it does so at the expense of ductility, reflecting a trade-off in which defects increase the critical stress for slip but reduce the critical strain at which slip initiates. The energy absorption capacity increases across all defect-containing models relative to the pristine case, with the 2-LT configuration showing the most substantial improvement. This highlights that the energy absorption capability is strongly governed by post-yield plastic deformation behavior.

3.2. *Strengthening mechanisms induced by twins and SFs*

Fig. 5 compares the strain accommodation by deformation mechanisms for each defect configuration, based on results from the model-2 case. The extent of each mechanism during post-yield was quantified, with the percent contribution to total strain accommodation determined by evaluating the strain tensors of atoms involved across the full deformation range. This approach enables a more detailed comparison of strengthening mechanisms between configurations with different types of defects. It should be noted that the percentages shown do not sum to 100 % because grain-elastic and purely elastic deformation contributions were not quantified [26].

In the defect-free case (Fig. 5a), strain accommodation at yield is dominated by the nucleation of Shockley partial dislocations forming intrinsic stacking faults (ISFs). A similar trend is observed in the 5-LT (Figs. 5c) and 4–3–2-GT (Fig. 5d) cases, both of which contain larger untwinned regions that readily facilitate Shockley partial dislocation nucleation. In contrast, deformation in the 2-LT (Fig. 5b), 4-LSF (Fig. 5e), and 6-LSF (Fig. 5f) cases is dominated either by the formation of multilayer stacking faults (MSFs) or by continued strain accommodation within pre-existing annealing twins.

In the 2-LT case (Fig. 5b), strain is primarily accommodated by twinning, which remains dominant until ~13 % strain, beyond which MSFs and partial dislocation slip prevail. By comparison, twinning contributions remain low throughout the deformation in the 5-LT (Figs. 5c) and 4–3–2-GT (Fig. 5d) cases, where strain accommodation transitions quickly to ISFs and MSFs after yield. This immediate shift indicates that the twinning grains in these cases primarily accommodate elastic strain rather than sustained plastic flow. The 2-LT configuration is the only case where twinning dominates beyond yield, supporting the conclusion that a higher density of twins significantly enhances strength, more effectively than dislocation–dislocation interactions alone.

It should be noted that several of the plots in Fig. 5 show a nonzero defect fraction at zero strain, followed by a sharp drop upon loading. This behavior is an artifact of the post-processing procedure, in which pre-existing defects in the initial configuration are subtracted to quantify only newly generated defects. Consequently, the apparent drop to zero does not indicate the annihilation of defects or physical disappearance but rather reflects the data normalization process. This artifact does not affect the subsequent analysis or interpretation of deformation mechanisms.

Fig. 6 compares and illustrates the deformation mechanisms across all defect configurations at a strain of 10 %. To facilitate discussion of individual grains, they are numbered as shown in Fig. 6a. In the defect-free model (Fig. 6a), deformation is predominantly governed by extensive partial dislocation slip, leading to the formation of a large number of HCP SFs. Dislocations nucleate at GBs, and glide along specific crystallographic planes. Since grain orientations are randomly assigned, the observed slip planes provide valuable insight into the active slip systems, serving as references for evaluating how dislocation motion is interrupted in the defect-containing models. In certain grains, such as grains 4 and 8, partial dislocations propagate preferentially along a single plane, consistent with activation of the {111}⟨110⟩ primary slip system when the loading direction aligns with the ⟨100⟩ orientation. In other grains, including grains 1, 5, 7, and 11, fewer partial dislocations

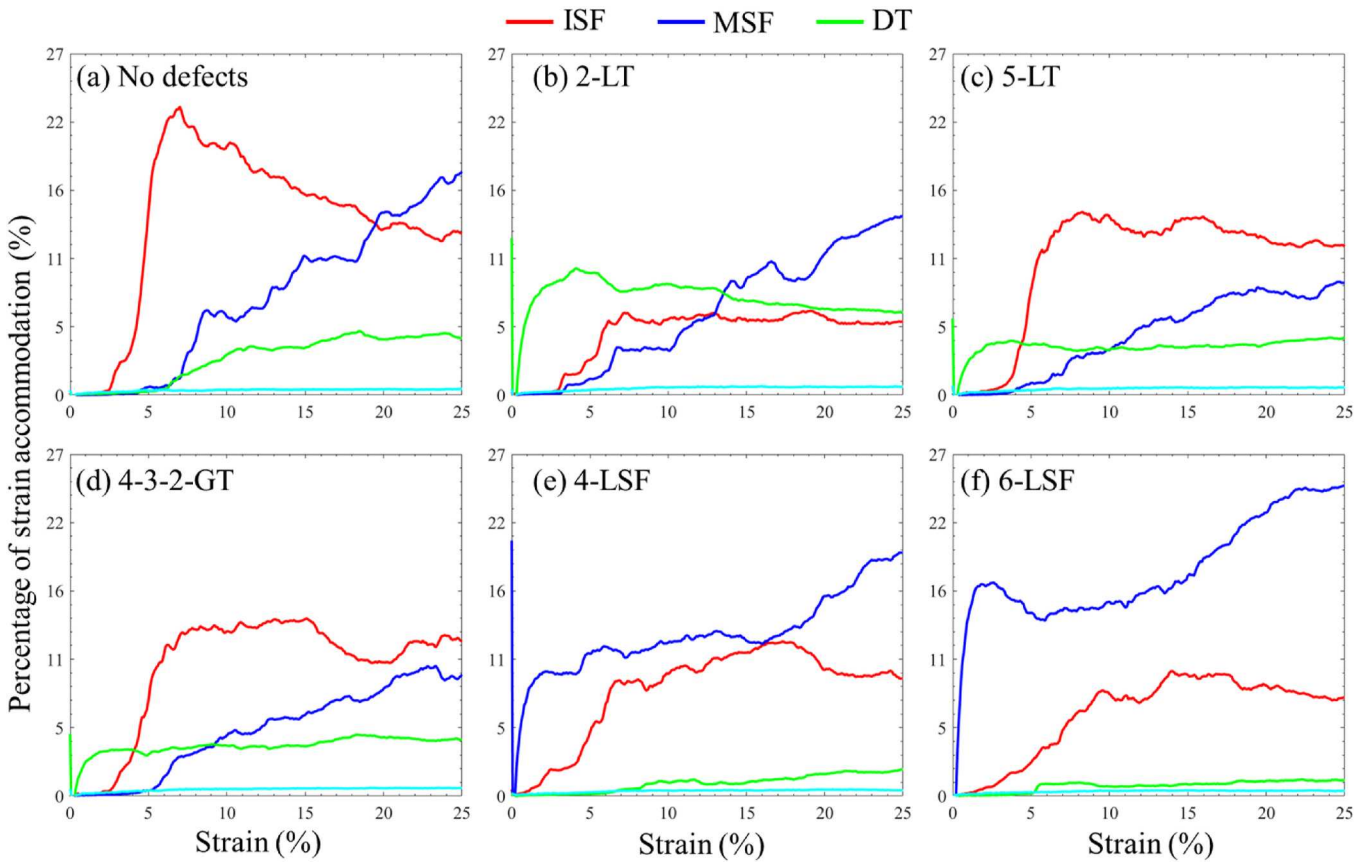

Fig. 5. Comparison of the percentage of total strain accommodation contributed by different deformation mechanisms in polycrystalline CrCoNi MEAs: (a) defect-free, (b) 2-atomic-layer twins, (c) 5-atomic-layer twins, (d) 4-2-3-atomic-layer gradient twins, (e) 4-atomic-layer SFs, and (f) 6-atomic-layer SFs. The red line denotes the fraction of atoms in intrinsic stacking faults (ISFs), the blue line represents the fraction of atoms in multilayer stacking faults (MSFs), and the green line indicates the fraction of atoms involved in deformation twinning (DT). (For interpretation of the references to color in this figure legend, the reader is referred to the Web version of this article.)

are observed, and slip is less uniform. For example, in grain 5, dislocations propagating along different directions intersect to form a locked triangular configuration. Such dislocation intersections, entanglements, and cross-slip events reach their maximum intensity in grains 9 and 12, where competing secondary slip planes with similar resistance energies are activated. These interactions produce sessile dislocations, such as Hirth and Lomer–Cottrell locks, which have also been experimentally observed in CrCoNi MEAs as important strengthening mechanisms [6, 10].

In comparison, the 2-LT case (Fig. 6b) exhibits a reduced degree of partial dislocation slip and minimal dislocation reactions. Deformation twinning (blue atoms), particularly wide twins, becomes the dominant deformation mode, consistent with the conclusions drawn from Fig. 5b. Partial dislocations are primarily observed gliding along twin boundaries (TBs). In some grains, such as grains 2 and 6, certain dislocations glide at an angle relative to the TBs; their motion ultimately terminates at the TBs rather than crossing. The high strength associated with the 2-LT case arises from the inhibition of dislocation motion by nanotwins, which restrict deformation and dislocation glide. Furthermore, because dislocation motion is confined between parallel twins, HCP phase regions are detected, as indicated by yellow arrows in Fig. 6b. These FCC–HCP phase transformations originate at GBs and propagate between deformation twins.

With the increase of the twin width, as in the 5-LT and 4–3–2-GT cases shown in Fig. 6c and d, both the number and width of deformation twins are significantly reduced compared to the 2-LT case (Fig. 6b), while partial dislocation activity increases. In these wider-twin configurations, dislocations are observed to glide along the twin lattice, as seen in grain 11, a behavior that is suppressed in the 2-LT case, indicating that a minimum spacing is required for dislocation motion. The increased spacing promotes more frequent nucleation and propagation of partial dislocations, which subsequently elevates the occurrence of dislocation–dislocation interactions that contribute to strengthening. Furthermore, in comparison to the defect-free case (Fig. 6a), pre-existing twins and deformation twins interact with dislocations and compel them to alter their glide paths, which further strengthens the alloy.

In the 4-LSF and 6-LSF cases (Fig. 6e and f), the deformation behavior differs from that of the twinned models. Extensive formation of stacking faults (SFs) is observed, and as the width of the pre-introduced SFs increases, both the number and thickness of newly generated SFs rise significantly. This evolution suppresses dislocation nucleation and propagation. In the 6-LSF case, the narrower spacing between adjacent SFs provides an additional barrier to dislocation motion. Together, these effects account for the higher strength observed in the 6-LSF case compared to the 4-LSF case (Fig. 4c).

These results suggest that two primary factors lead to increased strength: (i) the confinement and interruption of dislocation motion by twins, which restrict glide, promote FCC–HCP phase transformations,

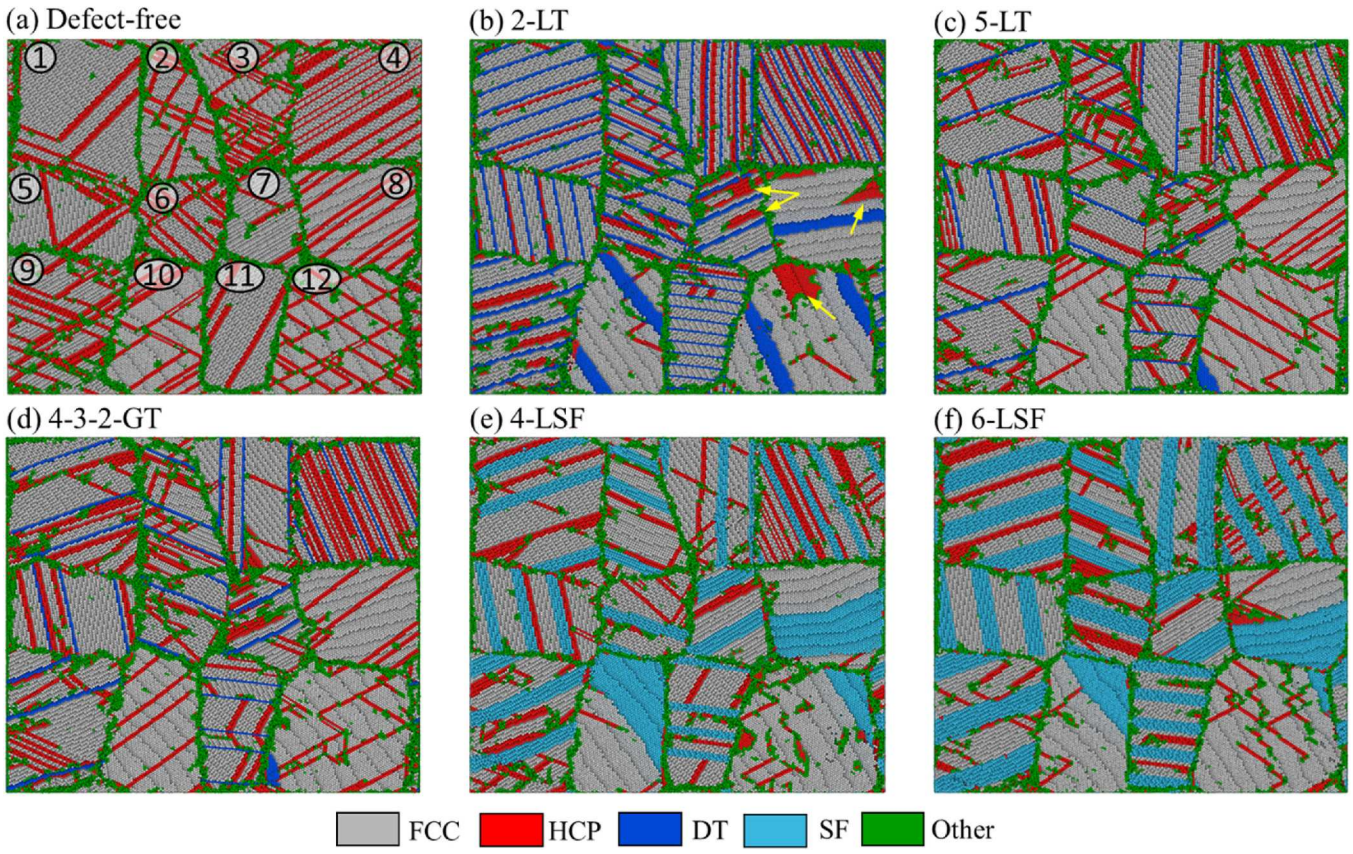

Fig. 6. Snapshots of deformed configurations for CrCoNi MEAs at a strain of 10 % for different defect conditions: (a) defect-free, (b) 2-atomic-layer twins, (c) 5-atomic-layer twins, (d) 4–3–2 atomic-layer gradient twins, (e) 4-atomic-layer stacking faults (SFs), and (f) 6-atomic-layer SFs.

and increase dislocation interactions; and (ii) the suppression of dislocation nucleation and propagation by stacking faults, where narrower inter-fault spacing further enhances resistance to plastic deformation. Thus, the 2-LTE and 6L-MSF cases resulted in the greatest strengthening benefit, as both configurations most effectively restrict dislocation motion.

To investigate the effect of pre-existing twin width on the evolution of deformation mechanisms, which are primarily deformation twinning and partial dislocation activity in the studied cases, we tracked and compared the deformation configurations of models with 2-atomic-layer and 5-atomic-layer twins. The 4–3–2 gradient twin case is not shown, as it exhibits similar mechanical properties (Fig. 4b) and deformation behavior (Fig. 6c and d) to the 5-atomic-layer twin case. Snapshots were selected immediately before and after the stress peak at $\varepsilon = 5$ %. As shown in Fig. 7a–d, deformation twinning is activated after yielding and serves as the primary work-hardening mechanism. This observation suggests that pre-introduced twins increase the energy barrier for dislocation nucleation; consequently, deformation twinning, which requires less energy to initiate, is activated. A comparison of Fig. 7a and d indicates that thinner twins, i.e., a higher density of twin boundaries (TBs), provide more nucleation sites for twinning. The reduced spacing also facilitates twin coalescence, ultimately leading to the formation of thicker twins (Fig. 7a).

Tracking the deformation sequence in the 2-atomic-layer twin case (Fig. 7a–c) shows that partial dislocations are initially activated until the dislocation density saturates, after which HCP phases nucleate and grow at relatively large strains. This mechanism accounts for the high energy absorption capability and sustained plastic flow stress observed in this configuration. By contrast, in the 5-atomic-layer twin case, only partial dislocations are observed, leading to lower energy absorption in the plastic flow regime (Fig. 4d).

To study the effect of SF thickness on the evolution of deformation mechanisms, we compared the deformation configurations of the 4-LSF and 6-LSF cases (Fig. 8). In both cases, SF formation and growth are favored over dislocation activity. A thicker pre-introduced SF promotes the nucleation of additional SFs, both in number and thickness. Similar to the pre-twinned models, partial dislocations tend to glide along SF boundaries, reflecting the lower energy barrier along these paths. However, with increasing SF thickness, dislocations were also observed to impinge upon and even traverse the SFs (grain 4). This behavior helps to explain the enhanced strength and ductility observed in the 6-LSF case compared with the 4-LSF case (Fig. 4).

3.3. *Effects of short-range order (SRO) on mechanical properties*

The calculated mean Warren–Cowley parameters, shown in Fig. 9, were used to characterize the generation of SRO in the CrCoNi MEA. Large positive values between like atoms (e.g., Ni–Ni) indicate strong clustering, whereas large negative values between unlike atoms (e.g., Co–Cr) also signify clustering. In contrast, large positive values between unlike atomic species suggest an absence of clustering between those pairs, while values near zero reflect a random distribution. The results reveal pronounced clustering effects for Ni–Ni and Co–Cr pairs, along with a lack of clustering between Ni–Co and Ni–Cr pairs. These findings

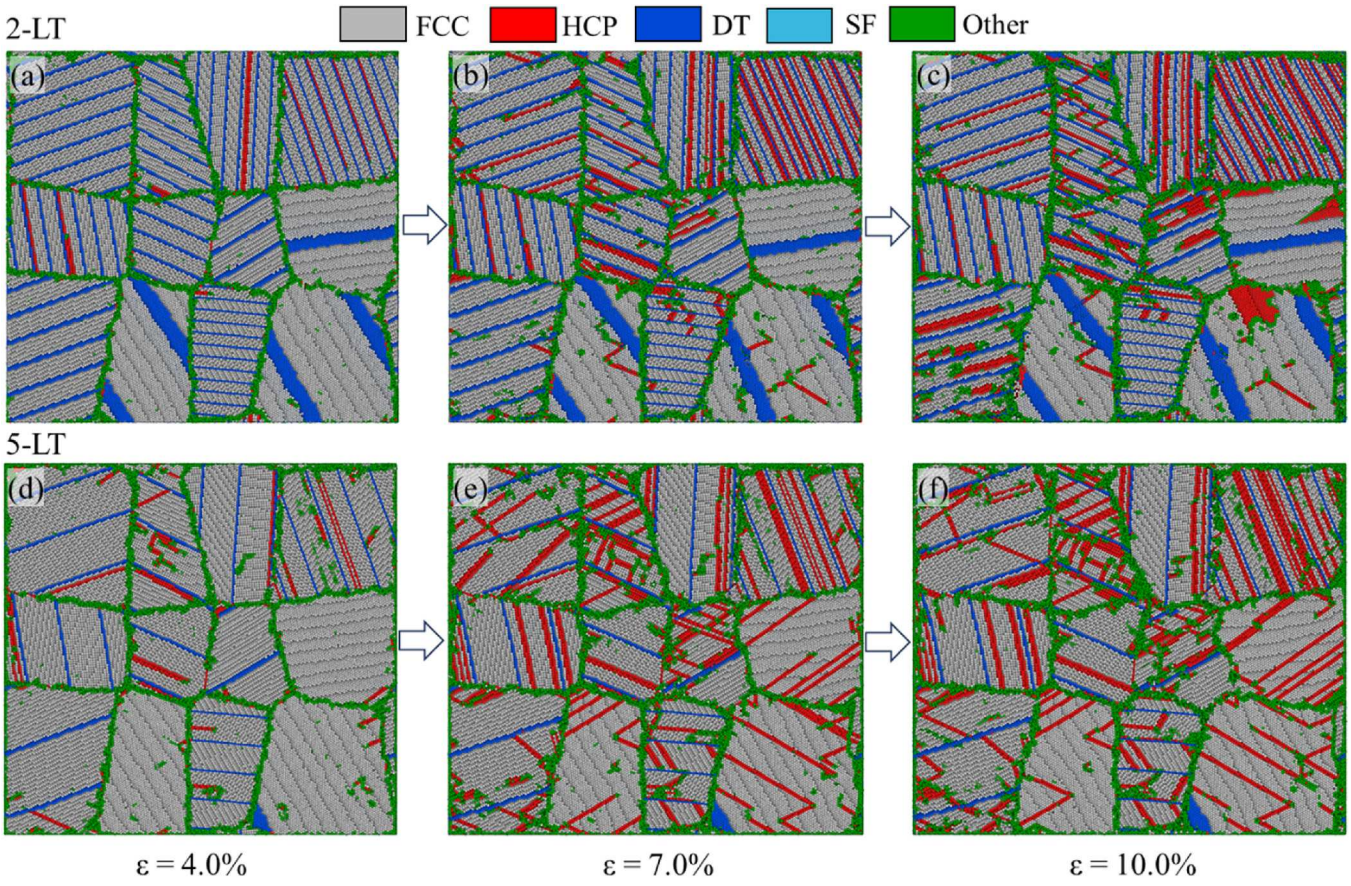

Fig. 7. Evolution of deformation twinning and dislocation motion in models with (a–c) 2-atomic-layer twins, (d–f) 5-atomic-layer twins at strains of 4.0 %, 7.0 % and 10.0 %. Both models reach their ultimate strength at a strain of ~5 % as shown in Fig. 4b.

are consistent with previous MD predictions of SRO [23,26].

To examine the effect of SRO on microstructural evolution, we compared the initial configurations of all tested cases under two conditions: random solid solution (RSS) and with SRO (Fig. 10). In the FCC structure, white atoms highlight Ni–Ni clustering induced by SRO. The most notable effect is the segregation of Ni atoms to pre-existing twins and SFs, as shown in Fig. 10b' (red arrows). These regions are energetically less stable than the bulk matrix, and Ni segregation lowers their interfacial energy, thereby stabilizing the boundaries.

A second prominent effect is microstructural coarsening, where two grains with low-angle misorientation merge through an intermediate grain (shaded region in Fig. 10b–b'). Such SRO-induced grain growth was observed across all cases, including the defect-free model, and originates from the annealing cycles applied prior to Monte Carlo simulations to minimize system energy. This behavior is consistent with experimental observations of grain coalescence during high-temperature annealing [32]. The observed microstructural coarsening during SRO generation reflects a realistic annealing-induced evolution rather than a model artifact. As SRO typically forms under thermal treatment, its influence on mechanical properties cannot be decoupled from concurrent grain coalescence and defect redistribution. The resulting microstructure, therefore, represents a physically meaningful, thermodynamically consistent state of the annealed MEA.

Additionally, in the defect-free case (Fig. 10a'), newly formed SFs were generated during annealing (yellow and cyan atoms). In twinned models (2-LT, 5-LT, and 4–3–2-GT), additional annealing twins appeared (red ovals in Fig. 10c', d'). Furthermore, annealing facilitated the reabsorption of line defects into the matrix, as seen in the 4-LSF case (Fig. 10e'), where one MSF disappeared following SRO generation (arrows in Fig. 10e). This defect reduction is consistent with experimental findings in CrCoNi MEAs, where annealing cycles reduce SF density [53].

Fig. 11 compares the stress–strain responses of all tested models under RSS (solid lines) and SRO (dashed lines) conditions. To highlight the effect of SRO, the corresponding mechanical properties were extracted and plotted in Fig. 12 for direct comparison with the RSS cases. Remarkably, SRO exerts a pronounced influence on mechanical performance, particularly in enhancing stiffness, strength, and energy absorption. The most significant effect is observed in strength, with increases of 45 % in the 4–3–2-GT and defect-free cases. In contrast, strengthening from pre-introduced twins and SFs reaches a maximum of only ~16 % in the 2-LT case (Fig. 12c), highlighting the tremendous impact of SRO.

Comparable improvements were also evident in stiffness and energy absorption, with maximum enhancements of 28 % in the 6-LSF case (Figs. 12a) and 50 % in the defect-free case (Fig. 12d), respectively. Yield strain exhibited notable increases of 42 % in the defect-free model and 26 % in the 2-LT model, though only minor changes were observed in other cases, with even a slight reduction in the 6-LSF case (Fig. 12b). Overall, these results demonstrate that SRO significantly enhances the strength and stiffness of CrCoNi MEAs, with its strengthening effect further amplified in the presence of pre-existing twin or SF defects. As

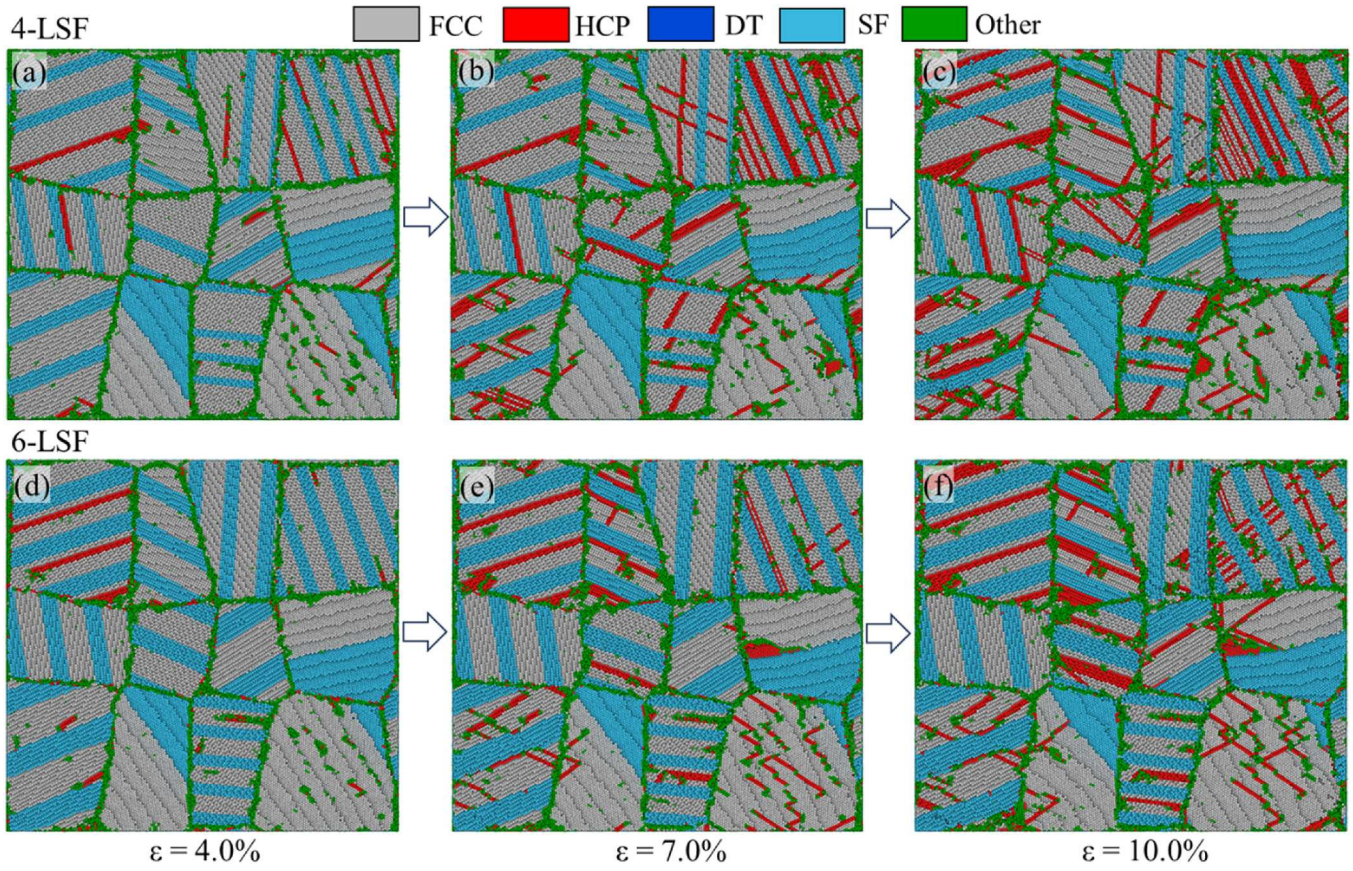

Fig. 8. Evolution of SF and dislocation motion in models with (a–c) 4-atomic-layer SFs and (d–f) 6-atomic-layer SFs at strains of 4.0 %, 7.0 % and 10.0 %. Both models reach their ultimate strength at a strain of ~5.5 % as shown in Fig. 4b.

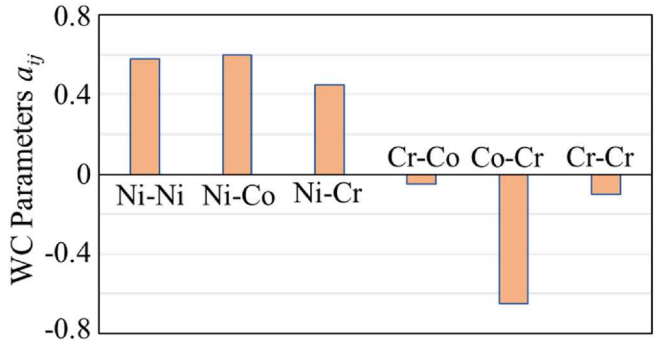

Fig. 9. Bar chart of the calculated Warren-Cowley parameters in this work, obtained using a modified Python script [52].

noted in Fig. 12c, the synergistic contribution of the 4–3–2 gradient twin and SRO yields a remarkable 57 % increase in strength.

3.4. SRO-induced strengthening mechanisms

In Fig. 13, we compared the strain accommodation of different defect configurations under RSS and SRO conditions. In the defect-free model, the presence of SRO reduced strain accommodation by partial dislocation slip, resulting in fewer ISFs, MSFs, and DTs compared to the RSS case. For the 2-LTE, 5-LTE, and 4–3–2-GT configurations, SRO similarly decreased the contribution from partial dislocations, while slightly enhancing strain accommodation from deformation twinning. In contrast, in models with pre-existing SFs, the introduction of SRO increased the strain accommodation from MSFs and DTs while reducing the contribution from isolated partial dislocation slip that generates ISFs.

To elucidate the underlying strengthening mechanisms, the deformed configurations of all test cases with SRO are presented in Fig. 14. Comparison with the RSS snapshots in Fig. 6 reveals several common phenomena. First, GB density is significantly reduced due to nanograin coalescence induced by SRO, as previously discussed. Second, the number of GB atoms decreases markedly in the SRO cases (Fig. 14). Since GBs are structurally weak regions with lower cohesive energy and act as preferential dislocation nucleation sites, their reduction leads to fewer opportunities for dislocation nucleation, explaining the lower dislocation density observed in SRO cases. Furthermore, fewer dislocation locks are formed under SRO, as indicated by circles in Fig. 14a compared to Fig. 6a, suggesting that SRO suppresses dislocation motion by increasing the barriers to glide.

The influence of pre-introduced twin and SF width is relatively minor compared to the effect of SRO. In the defect-free case (Fig. 14a), HCP phases and SFs formed during deformation (red and blue atomic regions). In the twinned cases, 2-LT, 5-LT, and 4–3–2-GT (Fig. 14b–d), both the number and width of deformation twins increased, but significantly fewer partial dislocations and HCP phases were generated. While some dislocations were observed gliding along twin boundaries, propagation between twins was largely inhibited. In the SF cases (Fig. 14e and f), stacking faults proliferated and became the dominant deformation mechanism, further suppressing dislocation nucleation. Fewer dislocations were observed gliding along SF boundaries in the SRO cases compared to RSS, and in some instances, their propagation paths were redirected across SFs (circled grain in Fig. 14e). Overall, GB reduction and the inhibition of dislocation activity induced by SRO are identified as the primary mechanisms responsible for the significant strengthening

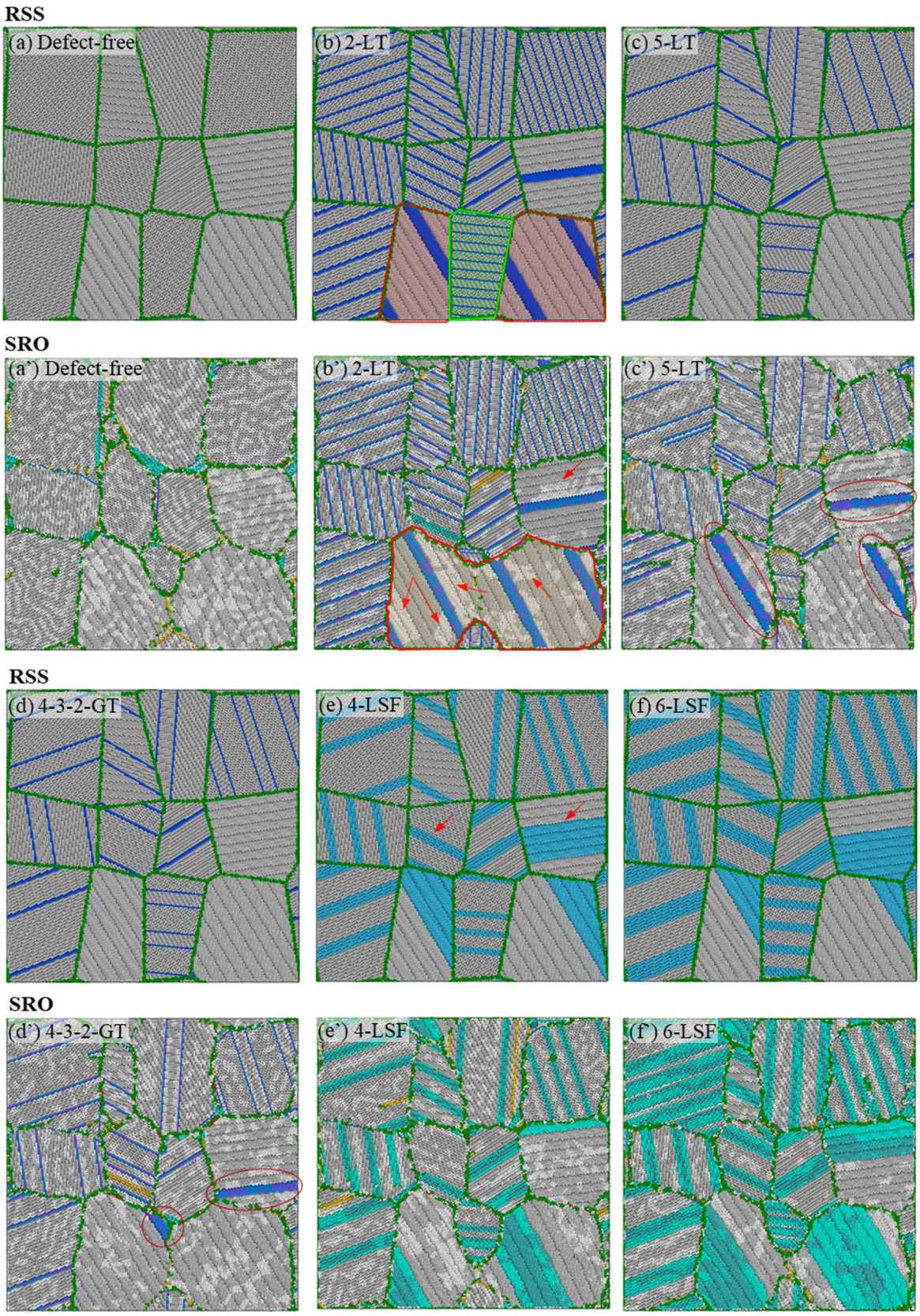

Fig. 10. Initial configurations of CrCoNi MEA models simulated as random solid solution (RSS) and with short-range order (SRO), under different defect conditions: (a, a') defect-free, (b, b') 2-atomic-layer twins, (c, c') 5-atomic-layer twins, (d, d') 4–3–2 atomic-layer gradient twins, (e, e') 4-atomic-layer stacking faults (SFs), and (f, f') 6-atomic-layer SFs. Primed panels represent models with SRO. Gray atoms correspond to FCC structures, dark blue atoms to annealing twins, cyan atoms to pre-existing SFs, and green atoms to amorphous structures. (For interpretation of the references to color in this figure legend, the reader is referred to the Web version of this article.)

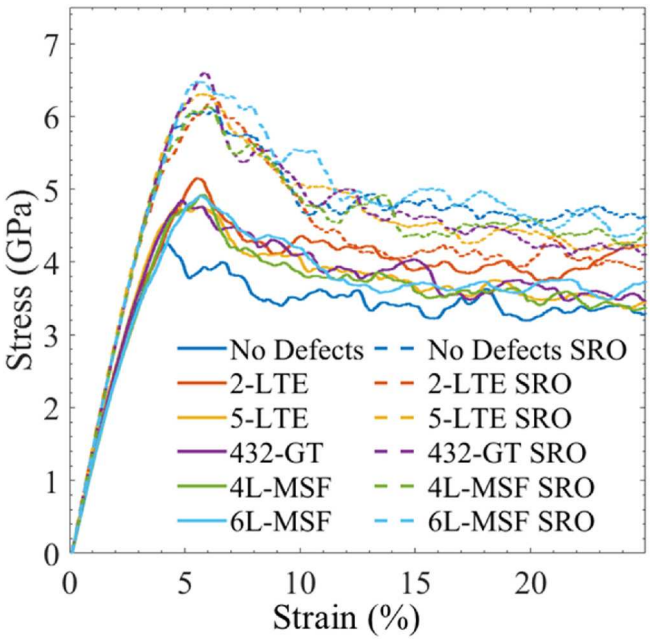

Fig. 11. Stress-strain responses of model-2 polycrystalline CrCoNi MEAs considering random solid solution (RSS) and with short-range order (SRO) with different defect types.

effect. The dislocation–twin boundary interactions, suppression of dislocation glide, and stacking fault evolution observed in Fig. 14 are consistent with experimental TEM and HT-TEM observations in CrCoNi and related MEAs [6,31–33]. These studies have reported similar twin-mediated strengthening, dislocation pinning at twin boundaries, and SRO-stabilized defect structures, supporting the mechanisms proposed in this work.

von Mises shear strain provides a scalar field that reflects the accumulated plastic shear and is directly correlated with dislocation pile-ups and slip bands. Therefore, Fig. 15 compares von Mises shear strain distribution for selected cases under RSS and SRO conditions, enabling clear visualization of localized deformation and dislocation pathways. As noted earlier, dislocation density in the SRO cases is significantly lower than in the RSS counterparts (Fig. 15a'-c' vs. Fig. 15a–c). Compared to RSS (Fig. 15a–c), von Mises strain in the SRO models is more spatially localized, with the exception of the defect-free case (Fig. 15a'). High-strain bands correspond to twin boundaries (TBs) in the twinned models (Fig. 15b–b') and to regions of dense stacking faults (SFs) in the SF models (Fig. 15c–c').

4. Conclusion

In this study, the effects of pre-existing planar defects of nanotwins and SFs, as well as SRO, on the mechanical properties and deformation mechanisms of polycrystalline CrCoNi MEAs under uniaxial tension were investigated by the atomistic simulation method.

Both nanotwins and SFs contribute significantly to strengthening in polycrystalline CrCoNi MEAs, though through distinct mechanisms. Nanotwins enhance strength by confining and interrupting dislocation glide, promoting FCC–HCP phase transformations, and increasing dislocation interactions, with thinner twins providing the greatest strengthening due to their higher twin boundary density. In contrast, SFs are strengthened by suppressing dislocation nucleation and propagation, with wider SFs producing more extensive faulting and narrower spacing creating stronger barriers to plastic deformation. Among these, the 2-atomic-layer twin and 6-atomic-layer SF configurations provided the most pronounced strengthening benefits.

Beyond planar defects, SRO was found to exert a far greater influence, enhancing strength by 45 %, stiffness by nearly 30 %, and energy

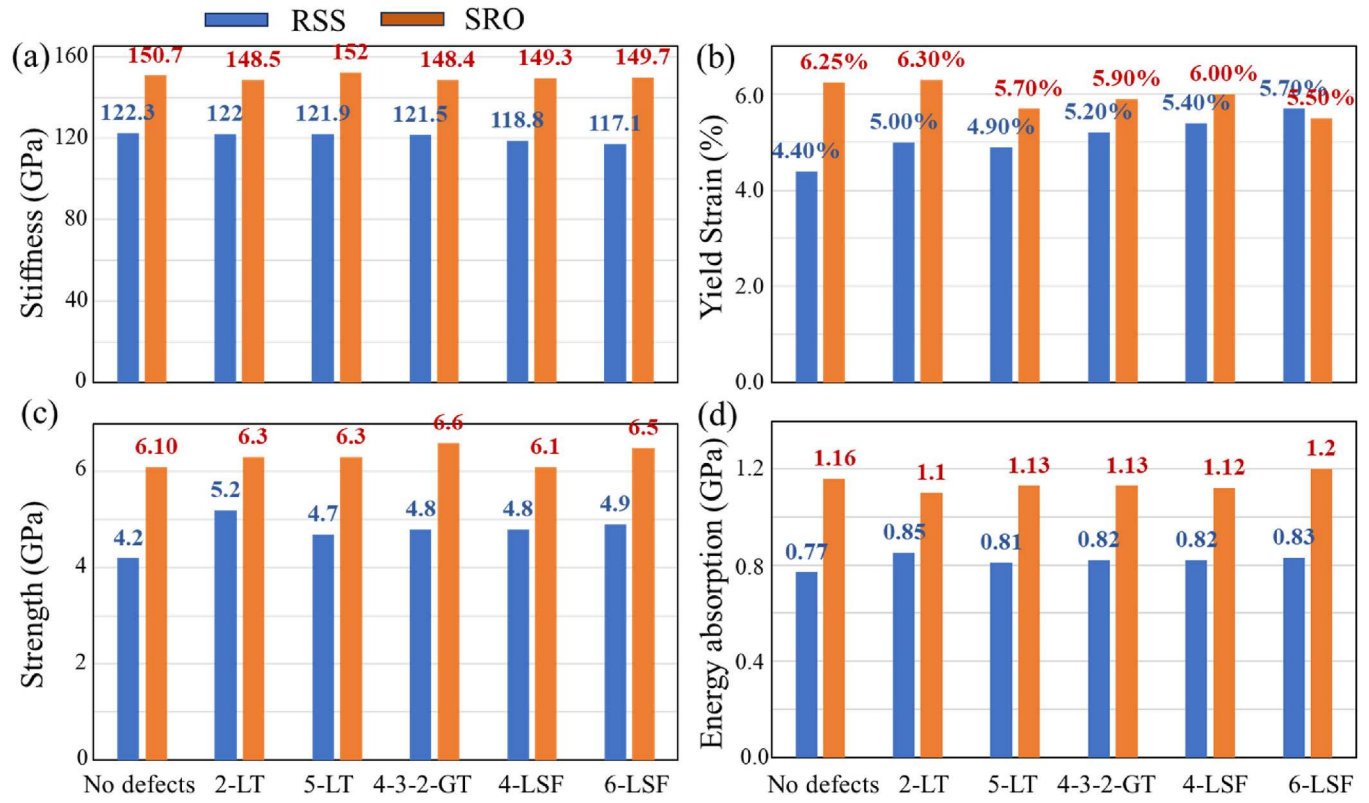

Fig. 12. Bar chart comparison of the mechanical properties of the model-2 polycrystalline CrCoNi MEA with different defect types: (a) stiffness, (b) yield strain, (c) strength, and (d) energy adsorption. The data were derived from the mean stress-strain curves in Figs. 11 and 3b.

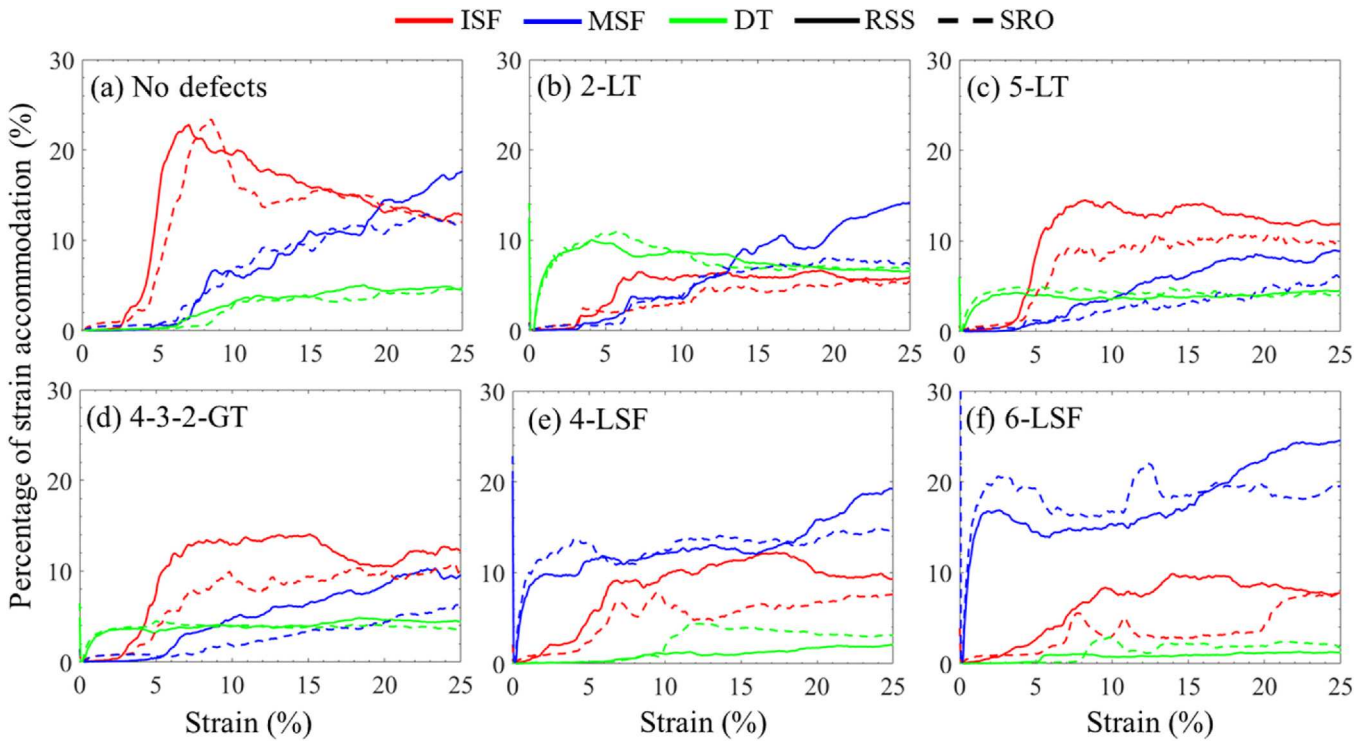

Fig. 13. Comparison of the percentage of total strain accommodation contributed by different deformation mechanisms in polycrystalline CrCoNi MEAs, with and without SRO: (a) defect-free, (b) 2-atomic-layer twins, (c) 5-atomic-layer twins, (d) 4-2-3-atomic-layer gradient twins, (e) 4-atomic-layer SFs, and (f) 6-atomic-layer SFs. Solid lines denote RSS cases, while dashed lines represent SRO cases.

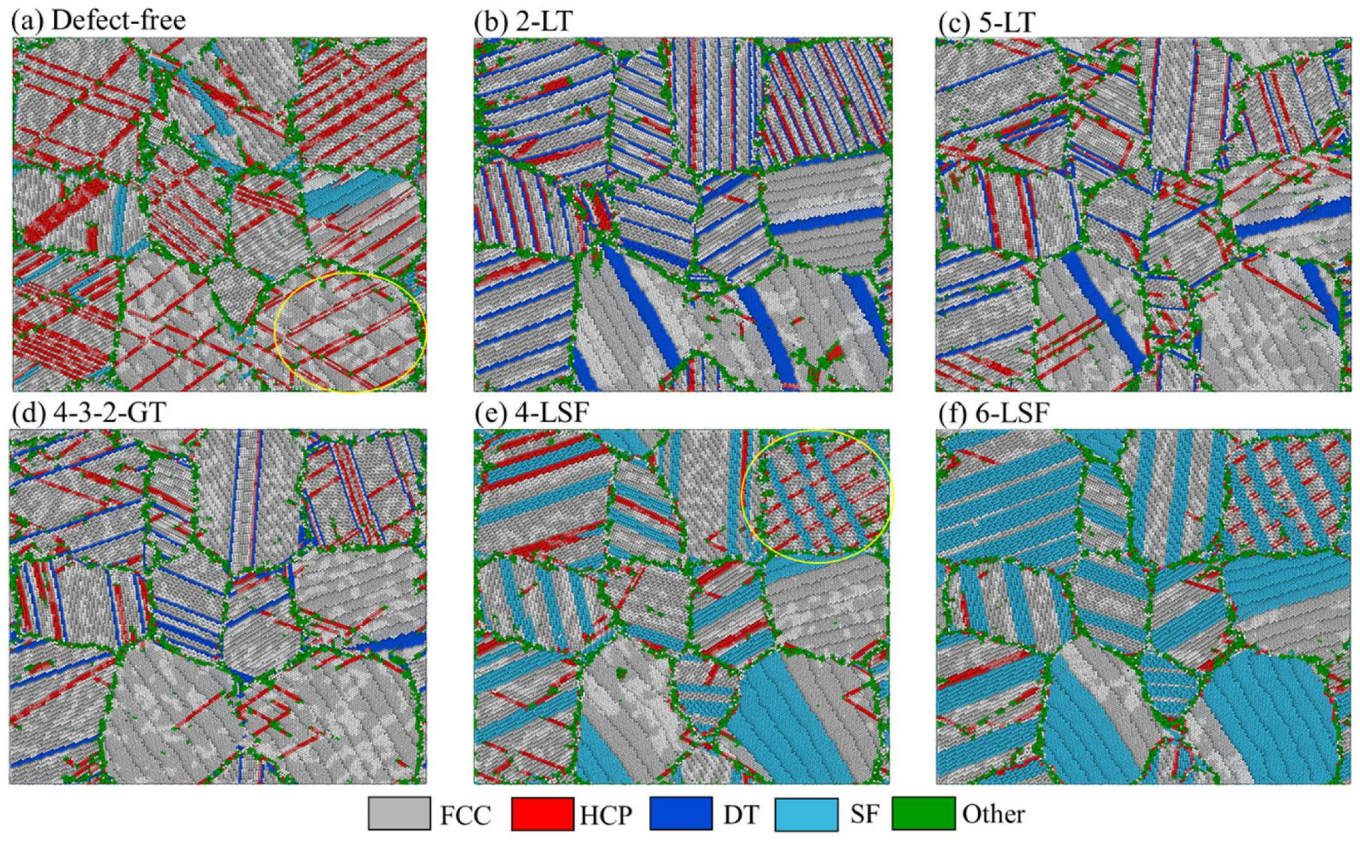

Fig. 14. Snapshots of deformed configurations for CrCoNi MEAs with SRO at a strain of 10 % for different defect conditions: (a) defect-free, (b) 2-atomic-layer twins, (c) 5-atomic-layer twins, (d) 4–3–2 atomic-layer gradient twins, (e) 4-atomic-layer stacking faults (SFs), and (f) 6-atomic-layer SFs.

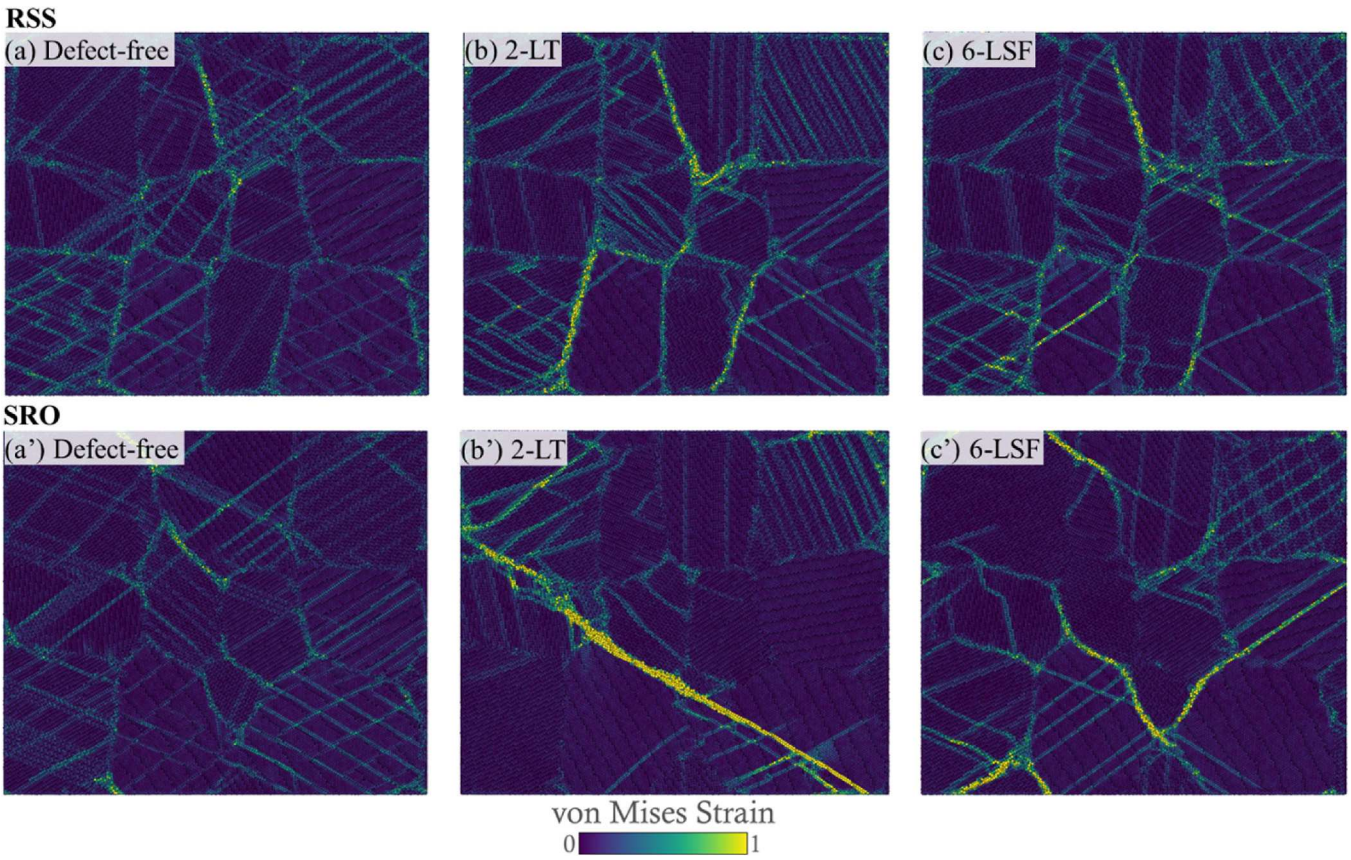

Fig. 15. Distribution of von Mises shear strain for selected cases under RSS and SRO conditions: (a, a') defect-free, (b, b') 2-LT, and (c, c') 6-LSF.

absorption by 50 %. The underlying mechanisms include stabilization of defect boundaries through Ni clustering, reduction of GB density via nanograin coalescence, and suppression of dislocation activity. Notably, when combined with gradient nanotwins, the strength of the alloy can be increased by as much as 57 %. Overall, while nanotwins and SFs provide important pathways for strengthening, SRO emerges as the most effective mechanism, with its effects further amplified in the presence of pre-existing planar defects.

While this work focuses on quantifying the macroscopic strengthening effects of SRO and planar defects on the mechanical response of CrCoNi MEAs, a more detailed atomic-scale investigation of dislocation-SRO interactions, such as local stress, energy landscape, and atomic configuration analyses, will be addressed in future work.

CRediT authorship contribution statement

Charles Matlock: Writing – original draft, Visualization, Validation, Software, Methodology, Formal analysis. **Ning Zhang:** Writing – review & editing, Supervision, Project administration, Methodology, Funding acquisition, Conceptualization.

Declaration of competing interest

The authors declare that they have no known competing financial interests or personal relationships that could have appeared to influence the work reported in this paper.

Acknowledgments

This work was supported by the Oak Ridge Associated Universities (ORAU) award number A21-0435, and the National Science Foundation under Award Numbers DMR-2316676 and CMMI-2302981. Simulations were performed at the High Performance and Research Computing Center at Baylor University and the ACCESS National Supercomputer Center.

Data availability

Data will be made available on request.

References

[1] J.-W. Yeh, Alloy design strategies and future trends in high-entropy alloys, Jom 65 (12) (2013) 1759–1771.
[2] D.B. Miracle, O.N. Senkov, A critical review of high entropy alloys and related concepts, Acta Mater. 122 (2017) 448–511.
[3] Z. Wu, H. Bei, G.M. Pharr, E.P. George, Temperature dependence of the mechanical properties of equiatomic solid solution alloys with face-centered cubic crystal structures, Acta Mater. 81 (2014) 428–441.
[4] A.M. Giwa, Z.H. Aitken, P.K. Liaw, Y.-W. Zhang, J.R. Greer, Effect of temperature on small-scale deformation of individual face-centered-cubic and body-centered-cubic phases of an Al0. 7CoCrFeNi high-entropy alloy, Mater. Des. 191 (2020) 108611.
[5] B. Gludovatz, A. Hohenwarter, K.V. Thurston, H. Bei, Z. Wu, E.P. George, R. O. Ritchie, Exceptional damage-tolerance of a medium-entropy alloy CrCoNi at cryogenic temperatures, Nat. Commun. 7 (1) (2016) 10602.
[6] G. Laplanche, A. Kostka, C. Reinhart, J. Hunfeld, G. Eggeler, E. George, Reasons for the superior mechanical properties of medium-entropy CrCoNi compared to high-entropy CrMnFeCoNi, Acta Mater. 128 (2017) 292–303.
[7] N. Li, J. Gu, B. Gan, Q. Qiao, S. Ni, M. Song, Effects of Mo-doping on the microstructure and mechanical properties of CoCrNi medium entropy alloy, J. Mater. Res. 35 (20) (2020) 2726–2736.
[8] D. Choudhuri, B. Gwalani, S. Gorsse, M. Komarasamy, S.A. Mantri, S.G. Srinivasan, R.S. Mishra, R. Banerjee, Enhancing strength and strain hardenability via deformation twinning in fcc-based high entropy alloys reinforced with intermetallic compounds, Acta Mater. 165 (2019) 420–430.
[9] Y. Ma, M. Yang, F. Yuan, X. Wu, Deformation induced hcp nano-lamella and its size effect on the strengthening in a CoCrNi medium-entropy alloy, J. Mater. Sci. Technol. 82 (2021) 122–134.
[10] Q. Ding, X. Fu, D. Chen, H. Bei, B. Gludovatz, J. Li, Z. Zhang, E.P. George, Q. Yu, T. Zhu, Real-time nanoscale observation of deformation mechanisms in CrCoNi-

based medium-to high-entropy alloys at cryogenic temperatures, Mater. Today 25 (2019) 21–27.
[11] Z. Pei, S. Zhang, Y. Lei, F. Zhang, M. Chen, Decoupling between Shockley partials and stacking faults strengthens multiprincipal element alloys, Proc. Natl. Acad. Sci. 118 (51) (2021) e2114167118.
[12] J. Yan, W. Fang, J. Huang, J. Zhang, R. Chang, X. Zhang, B. Liu, J. Feng, F. Yin, Plastic deformation mechanism of CoCrxNi medium entropy alloys, Mater. Sci. Eng., A 814 (2021) 141181.
[13] H. Jung, J. Lee, G.H. Gu, H. Lee, S.-M. Seo, A. Zargaran, H.S. Kim, S.S. Sohn, Multiscale defects enable synergetic improvement in yield strength of CrCoNi-based medium-entropy alloy fabricated via laser-powder bed fusion, Addit. Manuf. 61 (2023) 103360.
[14] D. Xu, M. Wang, T. Li, X. Wei, Y. Lu, A critical review of the mechanical properties of CoCrNi-based medium-entropy alloys, Microstructures 2 (1) (2022). N/A-N/A.
[15] P. Sathiyamoorthi, J.W. Bae, P. Asghari-Rad, J.M. Park, J.G. Kim, H.S. Kim, Effect of annealing on microstructure and tensile behavior of CoCrNi medium entropy alloy processed by high-pressure torsion, Entropy 20 (11) (2018) 849.
[16] H. Pommerenke, J. Duan, N. Curtis, V. DeLibera, A. Bratten, A. Hoffman, M. Buchely, R. O'Malley, H. Wen, A strong and ductile cobalt-free solid-solution Fe30Ni30Mn30Cr10 multi-principal element alloy from hot rolling, J. Alloys Compd. 948 (2023) 169566.
[17] J. Rackwitz, Q. Yu, Y. Yang, G. Laplanche, E.P. George, A.M. Minor, R.O. Ritchie, Effects of cryogenic temperature and grain size on fatigue-crack propagation in the medium-entropy CrCoNi alloy, Acta Mater. 200 (2020) 351–365.
[18] I. Weißensteiner, M. Petersmann, P. Erdely, A. Stark, T. Antretter, H. Clemens, V. Maier-Kiener, Deformation-induced phase transformation in a Co-Cr-W-Mo alloy studied by high-energy X-ray diffraction during in-situ compression tests, Acta Mater. 164 (2019) 272–282.
[19] R. Zhang, S. Zhao, J. Ding, Y. Chong, T. Jia, C. Ophus, M. Asta, R.O. Ritchie, A. M. Minor, Short-range order and its impact on the CrCoNi medium-entropy alloy, Nature 581 (7808) (2020) 283–287.
[20] L. Zhou, Q. Wang, J. Wang, X. Chen, P. Jiang, H. Zhou, F. Yuan, X. Wu, Z. Cheng, E. Ma, Atomic-scale evidence of chemical short-range order in CrCoNi medium-entropy alloy, Acta Mater. 224 (2022) 117490.
[21] Q. Ding, Y. Zhang, X. Chen, X. Fu, D. Chen, S. Chen, L. Gu, F. Wei, H. Bei, Y. Gao, Tuning element distribution, structure and properties by composition in high-entropy alloys, Nature 574 (7777) (2019) 223–227.
[22] X. Chen, Q. Wang, Z. Cheng, M. Zhu, H. Zhou, P. Jiang, L. Zhou, Q. Xue, F. Yuan, J. Zhu, Direct observation of chemical short-range order in a medium-entropy alloy, Nature 592 (7856) (2021) 712–716.
[23] Q.-J. Li, H. Sheng, E. Ma, Strengthening in multi-principal element alloys with local-chemical-order roughened dislocation pathways, Nat. Commun. 10 (1) (2019) 3563.
[24] S. Dasari, A. Sharma, C. Jiang, B. Gwalani, W.-C. Lin, K.-C. Lo, S. Gorsse, A.-C. Yeh, S.G. Srinivasan, R. Banerjee, Exceptional enhancement of mechanical properties in high-entropy alloys via thermodynamically guided local chemical ordering, Proc. Natl. Acad. Sci. 120 (23) (2023) e2211787120.
[25] H. Liu, B. Chen, R. Chen, J. He, D. Kang, J. Dai, Computational simulation of short-range order structures in high-entropy alloys: a review on formation patterns, multiscale characterization, and performance modulation mechanisms, Adv. Phys. X 10 (1) (2025) 2527417.
[26] A. Gupta, W.-R. Jian, S. Xu, I.J. Beyerlein, G.J. Tucker, On the deformation behavior of CoCrNi medium entropy alloys: unraveling mechanistic competition, Int. J. Plast. 159 (2022) 103442.
[27] C. Matlock, N. Zhang, Nanoscale deformation mechanisms in CrCoNi medium entropy alloys: influence of crystallographic orientation and chemical short-range order, Eur. J. Mech. Solid. (2025) 105762.
[28] Y. Wu, F. Zhang, X. Yuan, H. Huang, X. Wen, Y. Wang, M. Zhang, H. Wu, X. Liu, H. Wang, Short-range ordering and its effects on mechanical properties of high-entropy alloys, J. Mater. Sci. Technol. 62 (2021) 214–220.
[29] S. Plimpton, Fast parallel algorithms for short-range molecular dynamics, J. Comput. Phys. 117 (1) (1995) 1–19.
[30] T.D. Nguyen, GPU-accelerated Tersoff potentials for massively parallel molecular dynamics simulations, Comput. Phys. Commun. 212 (2017) 113–122.
[31] S. Yuan, B. Gan, L. Qian, B. Wu, H. Fu, H.-H. Wu, C.F. Cheung, X.-S. Yang, Gradient nanotwinned CrCoNi medium-entropy alloy with strength-ductility synergy, Scr. Mater. 203 (2021) 114117.
[32] H. Huang, J. Wang, H. Yang, S. Ji, H. Yu, Z. Liu, Strengthening CoCrNi medium-entropy alloy by tuning lattice defects, Scr. Mater. 188 (2020) 216–221.
[33] H. Deng, Z. Xie, B. Zhao, Y. Wang, M. Wang, J. Yang, T. Zhang, Y. Xiong, X. Wang, Q. Fang, Tailoring mechanical properties of a CoCrNi medium-entropy alloy by controlling nanotwin-HCP lamellae and annealing twins, Mater. Sci. Eng., A 744 (2019) 241–246.
[34] P. Hirel, Atomsk: a tool for manipulating and converting atomic data files, Comput. Phys. Commun. 197 (2015) 212–219.
[35] A. Stukowski, Visualization and analysis of atomistic simulation data with OVITO–the Open visualization Tool, Model. Simulat. Mater. Sci. Eng. 18 (1) (2009) 015012.
[36] A. Stukowski, V.V. Bulatov, A. Arsenlis, Automated identification and indexing of dislocations in crystal interfaces, Model. Simulat. Mater. Sci. Eng. 20 (8) (2012) 085007.
[37] S. Yang, N. Zhang, Y. Chen, Concurrent atomistic–continuum simulation of polycrystalline strontium titanate, Philos. Mag. 95 (24) (2015) 2697–2716.
[38] N. Zhang, M.A. Zaeem, Understanding specimen-and grain-size effects on nanoscale plastic deformation mechanisms and mechanical properties of polycrystalline yttria-stabilized tetragonal zirconia nanopillars, Eur. J. Mech. Solid. 76 (2019) 80–90.
[39] D. Farkas, Grain boundary structure in high-entropy alloys, J. Mater. Sci. 55 (22) (2020) 9173–9183.
[40] E. Ma, C. Liu, Chemical inhomogeneities in high-entropy alloys help mitigate the strength-ductility trade-off, Prog. Mater. Sci. 143 (2024) 101252.
[41] D. Hua, Q. Zhou, Y. Shi, S. Li, K. Hua, H. Wang, S. Li, W. Liu, Revealing the deformation mechanisms of< 110> symmetric tilt grain boundaries in CoCrNi medium-entropy alloy, Int. J. Plast. 171 (2023) 103832.
[42] W.-R. Jian, Z. Xie, S. Xu, Y. Su, X. Yao, I.J. Beyerlein, Effects of lattice distortion and chemical short-range order on the mechanisms of deformation in medium entropy alloy CoCrNi, Acta Mater. 199 (2020) 352–369.
[43] M. Li, Y. Guo, W. Li, Y. Zhang, Y. Chang, Property enhancement of CoCrNi medium-entropy alloy by introducing nano-scale features, Mater. Sci. Eng., A 817 (2021) 141368.
[44] X. Sun, W. Liu, X. Yu, Y. Su, Y. Sun, G. Liu, Molecular dynamics study of the microstamping of TiAl6V4 alloy, J. Mol. Model. 30 (12) (2024) 399.
[45] J. Li, W. Lu, L. Liu, S. Huang, M. Ji, Y. Zhao, Molecular dynamics simulation of microstructural evolution and mechanical behavior of titanium alloy subjected to laser shock peening, Opt Laser. Technol. 175 (2024) 110748.
[46] N.E. Chowdhury, A. Jawad, A. Rahman, M.J.A. Khan, Multi-fidelity neural network–based prediction of tensile strength of high-entropy alloy (FeNiCoCrCu) using molecular dynamics data, J. Mol. Model. 31 (8) (2025) 1–9.
[47] B. Sadigh, P. Erhart, A. Stukowski, A. Caro, E. Martinez, L. Zepeda-Ruiz, Scalable parallel Monte Carlo algorithm for atomistic simulations of precipitation in alloys, Phys. Rev. B Condens. Matter 85 (18) (2012) 184203.
[48] J.M. Cowley, An approximate theory of order in alloys, Phys. Rev. 77 (5) (1950) 669.
[49] N. Zhang, M.A. Zaeem, Competing mechanisms between dislocation and phase transformation in plastic deformation of single crystalline yttria-stabilized tetragonal zirconia nanopillars, Acta Mater. 120 (2016) 337–347.
[50] N. Zhang, Y. Chen, Nanoscale plastic deformation mechanism in single crystal aragonite, J. Mater. Sci. 48 (2) (2013) 785–796.
[51] S. Nosé, A unified formulation of the constant temperature molecular dynamics methods, J. Chem. Phys. 81 (1) (1984) 511–519.
[52] K. Sheriff, Y. Cao, T. Smidt, R. Freitas, Quantifying chemical short-range order in metallic alloys, Proc. Natl. Acad. Sci. 121 (25) (2024) e2322962121.
[53] Z. Li, C.C. Tasan, K.G. Pradeep, D. Raabe, A TRIP-assisted dual-phase high-entropy alloy: grain size and phase fraction effects on deformation behavior, Acta Mater. 131 (2017) 323–335.